*Article*

# Idle Vibration Reduction of a Diesel Sport Utility Vehicle

**Seokwon Ryu [1], Dongju Kim [1], Booyoung Lee [2], Doohee Han [3], Insoo Jung [3] and Jintai Chung [1,4,\***

[1] Department of Mechanical Engineering, Hanyang University, Ansan 15588, Republic of Korea; rtjrd-njs23@hanyang.ac.kr (S.R.); dongju0605@hanyang.ac.kr (D.K.)
[2] Hankook Tire and Technology Company, Daejeon 34127, Republic of Korea; leebooyeong@hankook-tech.com
[3] Hyundai Motor Company, Hwaseong 18280, Republic of Korea; nehee@hyundai.com (D.H.); isjung@hyundai.com (I.J.)
[4] BK21 FOUR ERICA-ACE Center, Hanyang University, Ansan 15588, Republic of Korea
**\*** Correspondence: jchung@hanyang.ac.kr

**Abstract:** This paper presents a study on the idle vibration reduction of a diesel sport utility vehicle (SUV). To reduce idle vibration, the transmission paths of vibration from the engine to the driver seat floor were investigated with the vehicle components related to idle vibration. Furthermore, operational deflection shape (ODS) tests were conducted to visualize the vibration shapes during engine idling. Experimental modal analyses were performed to obtain the natural frequencies and mode shapes. Through the ODS and modal tests, the vibration characteristics of the diesel SUV during idling were identified. Considering these vibration characteristics, a multi-body dynamic model for the diesel SUV described by differential equations of motion was established to evaluate the idle vibration. To implement the dynamic model effectively, the equivalent stiffnesses and damping coefficients included in the model were determined experimentally or analytically. The established dynamic model was verified by comparing the natural frequencies and idle vibration levels between simulations. Using this dynamic model, we analyzed the effects of various design variables on idle vibration and obtained an optimal design for reducing the idle vibration level. Finally, we present a design guide to reduce the idle vibration for diesel SUVs.

**Keywords:** diesel sport utility vehicle (SUV); idle vibration; multi-body dynamic model; vibration reduction; vibration absorber

## 1. Introduction

In recent years, as enhancement of the driving experience and comfort of consumers become paramount, the reduction of vibrations in vehicles during engine idling has garnered significant research attention. The vibration during engine idling is transmitted from an operating engine to a passenger while a vehicle is stationary, which significantly influences the buying preference of consumers. The vibrations during engine idling are clearly perceived by passengers, which when large negatively impacts the passengers' impression of the vehicle. Such vibrations are dominated by low-frequency components, and differ from those caused by road and wind perturbations during driving. Moreover, because compression ignition-type diesel engines bear a substantially higher compression ratio than spark ignition-type gasoline engines, diesel engines exhibit remarkably larger vibrations during engine idling than gasoline engines. Accordingly, various methods have been studied extensively for the reduction of vibration in diesel vehicles during engine idling.

Fundamentally, the vibration occurring during engine idling can be reduced by minimizing the vibration of the engine and transmission, which act as vibration sources during engine idling. To this end, several researchers have reported on related and relevant topics. Zheng et al. [1] proposed an engine–transmission control approach to improve fuel economy during urban driving and reduce the engine vibrations transmitted to the passenger compartment. Kim and Park [2] introduced two intelligent control systems to

reduce the fluctuations in engine speed at idle conditions, namely, an evolutionary computing control based on genetic algorithms and a stochastic control based on the Alopex algorithm. Fu et al. [3] proposed a hybrid proportional electromagnetic dynamic vibration absorber comprising an electromagnetic actuator and an elastic element to control the engine vibration during idling. Moreover, Shen et al. [4] presented an experimental study on the first-order vibration improvement of a malfunctioning vehicle in development during the engine idle condition. They analyzed the generation mechanism of the first-order vibration problem during engine idling, and subsequently, experimentally derived the possible vibration excitation source and transfer path.

Recently, several studies have been conducted to reduce the vibration caused by the gear rattle in the transmission during idling [5–9]. Shangguan et al. [5] proposed a nonlinear torsional model of a driveline system to study the gear rattle during idling and advanced a design guideline for the selection of adequate clutch stiffness and damping properties of the clutch to reduce gear rattle. Yucesan and Sezer [6] employed an analytical model featuring a new time-varying gear mesh stiffness function to investigate the influence of the clutch disk mechanism on the rattle during engine idling. Based on the magnetorheological effect in elastomeric spring elements, Brancati et al. [7] developed a device housing a flywheel equipped with a torsional vibration damper, which can reduce the gear rattle of the flywheel in a low-speed regime. Chen et al. [8] conducted a study to reduce the vibration of a dual-mass flywheel torsional damper under multiple working conditions including ignition, idle, startup, and drive conditions

Excluding the engine and transmission, the vibration of vehicle components situated along the vibration path during engine idling have been minimized in numerous research. Among these studies, the studies related to mount structures have been most actively conducted. Choi and Song [9] proposed a magnetorheological engine mount for the vibration control of a vehicle and evaluated the vibration at the driver's position in the time and frequency domains. Azadi et al. [10] introduced a new engine mount with variable stiffness, which provides superior vibration control over that of a hydro-mount and a passive rubber mount under idling conditions. For vibration attenuation during engine idling, Guo and Zhou [11] developed a non-linear lumped-parameter model of a semi-active engine mount with air springs. To reduce the steering-wheel jitter of a commercial vehicle during engine idling, He et al. [12] studied the vibration isolation performance of a powertrain suspension system.

In addition, myriad researchers have attempted to reduce vibrations of vehicle parts other than engine mounts during engine idling. Lim et al. [13] proposed methods for reducing the transmitted vibration forces caused by the mass unbalance of the radiator cooling fan that occurs during vehicle idling. They demonstrated that the force of vibration of the cooling fan can be reduced by increasing the stiffness of the shroud stators and decreasing the stiffness of the rubber mountings. Wang et al. [14] put forward a half-vehicle suspension model with a double-delay feedback control to improve the vibration performance under idling conditions; the results indicate that the active suspension featuring time-delayed feedback control improved the vibration reduction.

Moreover, researchers have explored various methods to reduce the vibration transmitted to the passenger compartment or the steering wheel during engine idling. Bohn et al. [15] presented an approach for the active control of a vehicle subjected to harmonic disturbances with time-varying fundamental frequencies. Using this approach, they significantly reduced the sound and vibration levels within the passenger compartment during engine idling. Han et al. [16] investigated the cause of severe vibration of a vehicle with a four-cylinder engine under engine idling conditions and presented an improved structural design of the vehicle floor to avoid the occurrence of resonance. To reduce the vibration of the steering column during engine idling, Kim and Kim [17] developed an optimal design process for steering column and supporting systems. To improve the overall performances of an automotive steering system, Wang et al. [18] studied the performance of the steering system in terms of steering feel, sensitivity, and modality, and reduced the engine vibration at idle condition. Considering the coupling effect of the multi-

source vibration transfer paths, He et al. [19] introduced a multi-point iterative analysis method to reduce the total vibration of the steering wheel at idle speed. To solve the vibration problem of an automotive steering wheel under idling condition, Tang et al. [20] proposed a multi-node joint vibration control strategy on the basis of the associated vibration path of the steering wheel.

Although several researchers have sufficiently improved the idling engine vibration condition for passenger cars, the vibration from diesel sport utility vehicles (SUVs) remains a matter of dissatisfaction for consumers. To effectively reduce the idling engine vibration of SUVs, a systematic approach, which can clearly analyze the source and transmission path of this vibration using mathematical modeling, is required. In prior studies, researchers have attempted to reduce idling engine vibrations by targeting specific parts of the vehicle, such as the engine, transmission, mount, body floor, and steering wheel, without considering the entire transmission path of the vibrations. However, not only the aforementioned parts, but also the radiator, intercooler, and front-end module are present in the transmission path of the vibrations; thus, these parts should be considered to reduce the idling engine vibration of diesel SUVs. To the best of the authors' knowledge, studies on the reduction of idling engine vibration, wherein all the parts on the transmission path of the vibration were considered, have not been attempted as yet; this is a challenging task because of the complexity of the connecting structures and supporting conditions of these parts. Accordingly, in this study, we established a dynamic model including those parts on the transmission path of vibration for a diesel SUV and reduced the idling engine vibration by implementing an optimal design based on the established model. The approach presented in this study can effectively improve the idling vibration of a diesel SUV and reduce the time and cost involved in the development or design stage.

The contents of this paper aimed at the analysis and reduction of the idling engine vibration of a diesel SUV are as follows. In Section 2, the analysis results of the idling vibration have been presented; an operational deflection shape (ODS) analysis was performed to observe the dynamic deformation of the SUV during engine idling. In addition, an experimental modal analysis was performed for the SUV components related to idling vibration. The experimental and analytical methods to obtain various modeling parameters, including the engine excitation force as well as the stiffness and damping properties of the bushings and hoses, are presented in Section 3. In Section 4, a dynamic model to predict idle vibration has been established for the diesel SUV; this model was verified by comparing the computational and experimental results. To identify the major design factors that considerably influence the idling vibration, a parametric study on various design factors was conducted, as presented in Section 5. Based on the results of this study, an optimal design featuring significant design factors was obtained to reduce the idling vibration, and a design guide for reducing the idling vibration has been proposed. Finally, the results and conclusions of this study have been summarized in Section 6.

## 2. Experimental Analysis

The paths through which the idling vibration is transmitted were identified prior to the experimental analysis of the dynamic behavior of a diesel SUV during engine idling. The diesel SUV considered in this study possessed a transverse-mounted four-cylinders engine driven by its front wheels; this SUV produced considerable vibrations that were perceivable to the passenger. Generally, the powertrain (i.e., the engine and transmission) of the transverse engine is placed parallel to the driving axis of the front wheels. To identify the transmission paths, automotive parts related to the transmission of vibrations were selected, and the connecting structures of these parts were analyzed in terms of their dynamics. As shown in Figure 1, the main components on the transmission paths from the idling engine that generates vibrations to the floor of the driver's seat are the powertrain, radiator, intercooler, front end module (FEM) carrier, side member, cross member, and the body floor. The $x$-, $y$-, and $z$-axes represent the longitudinal, transverse, and vertical directions of the vehicle, respectively.
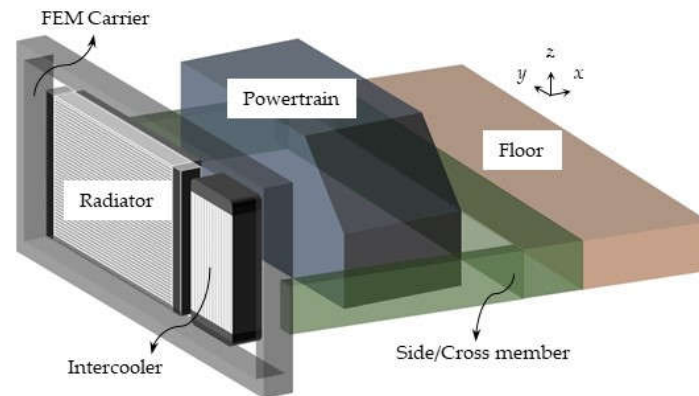
**Figure 1.** Components of a diesel SUV on the transmission paths of idling vibration.

The vibrations produced by the idling engine are mainly transmitted along two paths from the engine to the body floor, as shown in Figure 2. The first path lies through the mounts of the powertrain, whereas the second path lies through the radiator or intercooler. First, the powertrain mount serves as the path through which the vibration is transmitted sequentially from the powertrain, three mounts, the front side member, and the body floor. The side member structurally supports the powertrain and imparts strength and rigidity to the front body. The powertrain mounts reduce the idling vibrations caused by the explosive force of engine, which are transmitted to the body floor. The powertrain used in this study is supported at three points by an engine mount, a transmission mount, and a roll mount. Herein, the engine and transmission mounts are fixed to the right and left side members, respectively, and the roll mount is fixed to the cross member. The side and cross members are welded and strongly bonded to the body floor.
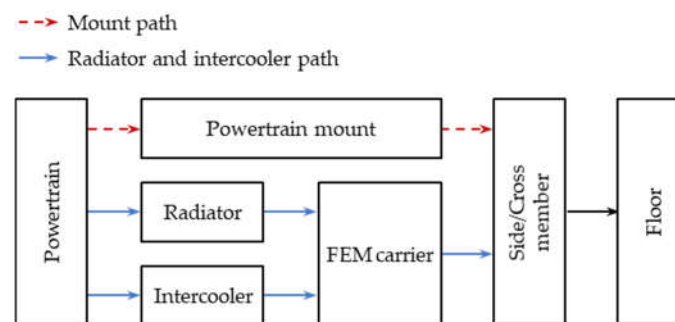


**Figure 2.** Transmission paths of idle vibration for the diesel SUV.

Further, the radiator/intercooler path consists of the powertrain, a radiator/intercooler, an FEM carrier, a side member, and the body floor. The cooling systems, i.e., the radiator and intercooler, which are located at the front of the powertrain, are connected to the engine through the inlet and outlet hoses. The hoses connecting the radiator and the powertrain are made of rubber, and the hoses connecting the intercooler and the powertrain are composed of plastic and rubber. In particular, the radiator and intercooler are mounted on the FEM carrier with rubber bushings. The radiator is connected to the FEM via two upper and two lower bushings, whereas the intercooler is connected to the FEM via one upper and two lower bushings. The FEM carrier is firmly bolted to the front of the side member.

When the engine is in an idle state, the dynamic behaviors of the powertrain, radiator, intercooler, and body, which are components of a diesel SUV, were investigated through an ODS analysis. The ODS represents the shape of a structure that has been deformed or set into motion by an excitation force, and it is generally used to analyze the shape deformation over time or at a specific frequency. To analyze the vibration of the SUV during engine idling, the dynamic deformation shapes of various vehicle parts at the excitation

frequency under idling conditions were obtained through ODS analysis. In this paper, the experimental method for the ODS analysis has been briefly described. Please refer to the concerned study [21] for more details on the ODS analysis and related experimental method.

To obtain the ODS's of the components, we used triaxial accelerometers (PCB 356A15) capable of sensing vibration signals in three mutually perpendicular directions. The accelerometers are attached to the measurement points to obtain the ODSs, as shown in Figure 3, wherein the squared and circled markers represent the measurement points for the reference and roving vibration signals, respectively. The reference signal was measured at the top end of the engine, whereas the roving signals were measured at the designated points to identify the behavior of each component. To obtain the ODS of the powertrain, vibration signals were measured at a total of eight points (four points at the top and four points at the bottom of the powertrain). To acquire the ODSs of the radiator and intercooler, vibration signals were measured at eight points, each with four vertices. Finally, vibration signals were measured at two points on each side member, a total of four points, and six points on the car body floor to analyze the ODS's of the side members and body floor.
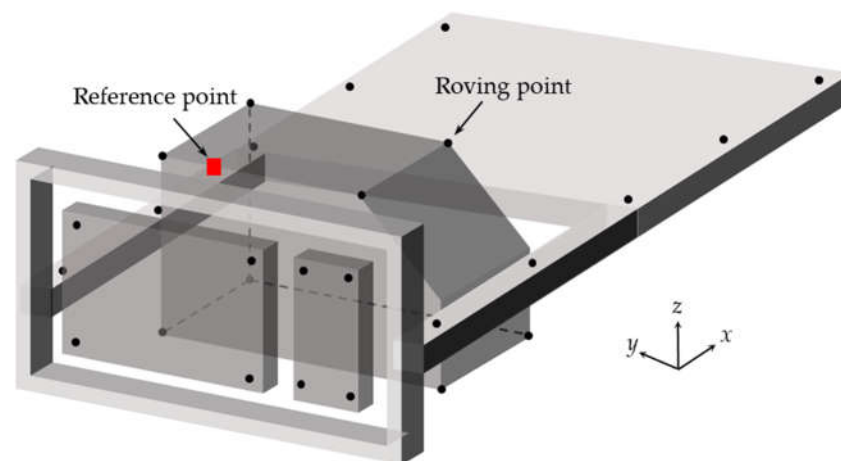


**Figure 3.** Measurement points of vibration signals to obtain ODSs.

The vibration signals measured by the accelerometers were analyzed by a sound and vibration analyzer (B&K 3560-D) with 60 channels to obtain the ODSs. The amplitudes and phases of auto-spectra and cross-spectra were obtained using the analyzer. Based on these measurements, the ODS frequency response functions of the roving signals with respect to the reference signal were extracted, and subsequently, the ODS of each component was derived. The ODSs were measured for an operating engine speed of 830 rpm in the idle engine state. Considering the four-cylinder diesel engine of the SUV, the excitation frequency emitted by the engine in the idle state was 27.7 Hz. The frequency spectra for vibration signals in the three mutually perpendicular directions at the position of the driver's seat on the body floor under idling engine conditions are depicted in Figure 4. As shown in this figure, the spectra exhibit large peaks at the idling frequency of 27.7 Hz.
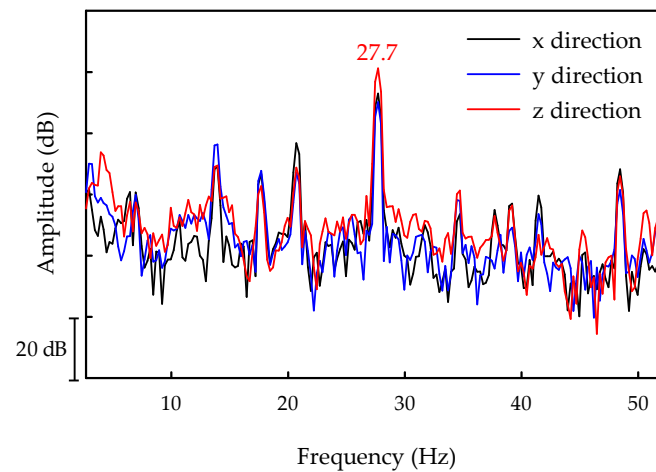
**Figure 4.** Frequency spectra of the vibration signals at the driver's seat on the body floor.

The ODSs of the powertrain, radiator, intercooler, and body floor of the SUV were analyzed at an engine excitation frequency of 27.7 Hz in the idle state (Figure 5). All motions appearing later are described based on the global coordinate system.
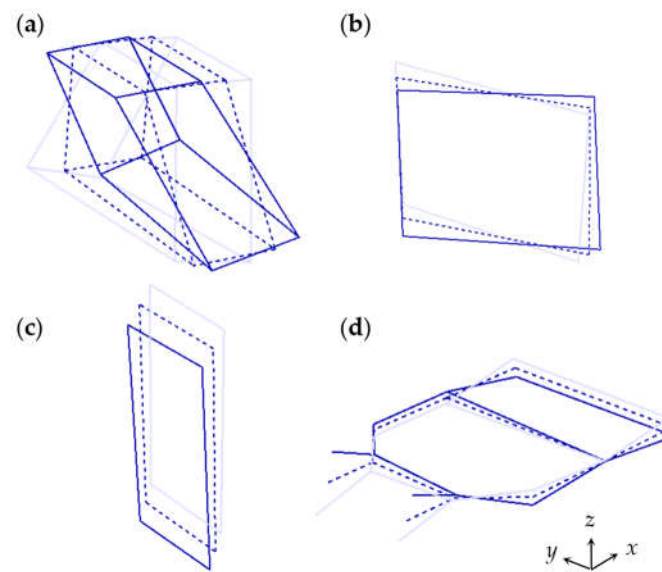


**Figure 5.** Operational deflection shapes of various components at the idling frequency of 27.7 Hz: (**a**) powertrain; (**b**) radiator; (**c**) intercooler; and (**d**) body floor.

First, as shown in Figure 5(a), the ODS of the powertrain exhibits a rotational vibration about the $y$-axis, which is generally called the pitch motion. This rotational vibration occurred because the SUV used in this study was driven by a transverse-mounted engine that generated a driving torque about the $y$-axis. Moreover, the ODS of the radiator, as illustrated in Figure 5(b), represents the vibration shape in which the rotational motion about the $x$-axis and the translational motion in the $x$ direction are combined. Because the rubber hoses attached to the upper left and lower right sides of the radiator are connected to the engine, the engine excitation force is transmitted through these hoses; accordingly, the combined motion of rotation and translation is represented in the ODS result depicted in Figure 5(b). Conversely, as shown in Figure 5(c), the ODS of the intercooler vibrates in the vertical direction with a slight longitudinal vibration. In other words, the intercooler possesses a vibration shape resembling that of a bounce motion when the engine is in the idle state. Because the hoses between the intercooler and the engine are connected almost

symmetrically to the top and bottom of the intercooler, this particular ODS was observed. Finally, the ODS of the vehicle body floor, as illustrated in Figure 5(d), appears in the shape of a combination of bending and torsional deformations. Furthermore, the bending deformation dominates over the torsional deformation. Notably, the ODS of the body floor suggests flexible-body motion, whereas the ODSs of the powertrain, radiator, and intercooler indicate rigid-body motions. Comparing the vibration amplitudes of the ODSs for these four components, the amplitude of the powertrain is the largest, followed by that of the intercooler, radiator, and body floor.

Modal tests were performed to obtain the natural frequencies and mode shapes of the powertrain, radiator, intercooler, and body floor under the condition that all the components are assembled together. The modal tests were conducted on the diesel SUV with all these components assembled; an impact hammer (B&K 8206) was used to apply input excitation, and accelerometers (PCB 356A15) were used to measure the output acceleration signals. Considering that the idle vibrations at the driver's seat occurred mainly in the vertical direction, vertical excitation was imposed on each component using the impact hammer to extract the natural frequencies and mode shapes related to vertical vibrations. The impact and measurement points for performing modal tests of each component are illustrated in Figure 6, wherein the red squares and circles represent the impact hammer excitation points and the accelerometer attachment positions, respectively. After obtaining a series of the frequency responses functions for each component using the sound and vibration analyzer, the natural frequencies and associated mode shapes were determined.
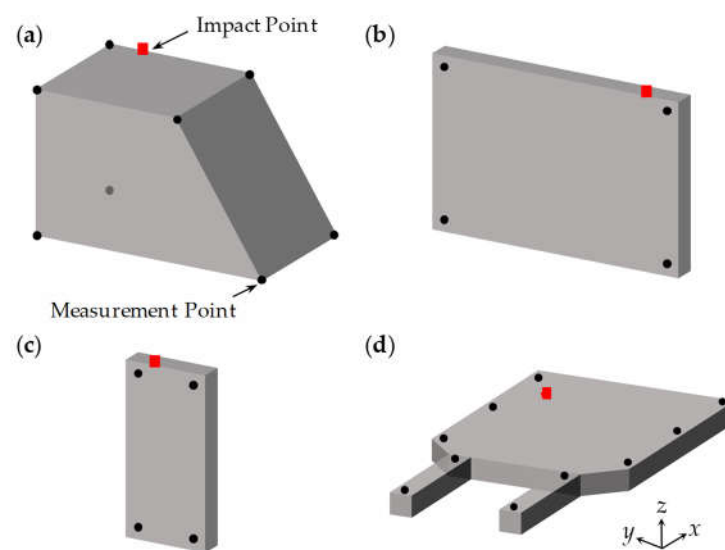


**Figure 6.** Impact and measurement points for the experimental modal tests: (**a**) powertrain; (**b**) radiator; (**c**) intercooler; and (**d**) body floor.

In this study, the natural frequencies and mode shapes of the components were chiefly analyzed in the low-frequency region. The vibration modes in the low-frequency region are closely related to the vibration in the idle state. The mode shapes of the powertrain, radiator, and intercooler in the low-frequency region are presented in Figure 7. The powertrain of the SUV employed in this study is supported by the engine, transmission and roll mounts. Because these mounts act as springs and dampers and support the powertrain, the powertrain exhibits six rigid-body vibration modes. The powertrain possesses the rigid-body modes corresponding to the natural frequencies of 4.8, 13.0, and 18.5 Hz. The mode for the natural frequencies of 4.8, 13.0, and 18.5 Hz are the bounce (refer to Figure 7(a)), pitch (refer to Figure 7(b)), and roll modes (refer to Figure 7(c)). In the low-frequency region during the idle state, three natural vibration modes of the radiator and intercooler exist, which are related to the ride comfort. These modes comprise the bounce

mode of the radiator with a natural frequency of 20.0 Hz (refer to Figure 7(d)), the roll mode of the radiator with a natural frequency of 30.3 Hz (refer to Figure 7(e)), and the bounce mode of the intercooler with a natural frequency of 29.3 Hz (refer to Figure 7(f)).
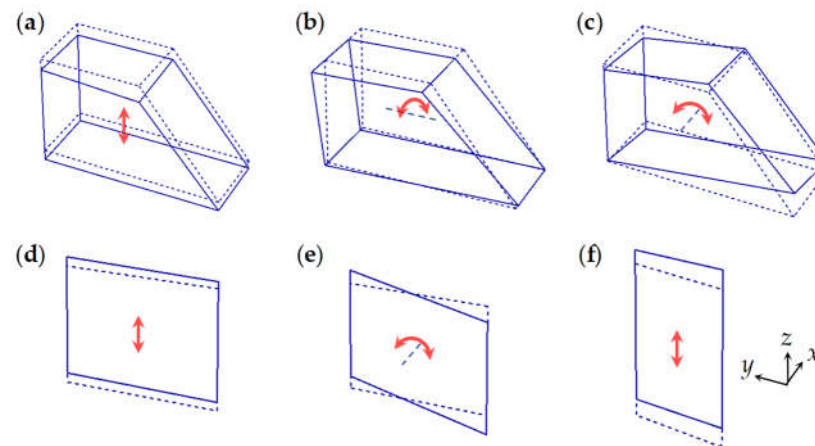


**Figure 7.** Mode shapes of the components: (**a**) bounce mode of the powertrain (4.8 Hz); (**b**) pitch mode of the powertrain (13.0 Hz); (**c**) roll mode of the powertrain (18.5 Hz); (**d**) bounce mode of the radiator (20.0 Hz); (**e**) roll mode of the radiator (30.3 Hz); and (**f**) bounce mode of the intercooler (29.3 Hz).

In the low-frequency region, unlike the powertrain, radiator, and intercooler, which solely exhibit rigid-body modes, the body floor possesses not only rigid-body modes but also deformed modes. The mode shapes for the four lowest natural frequencies of the body floor are depicted in Figure 8. The modes depicted in Figures 8(a) and 8(b) are rigid-body modes of the body, whereas the modes represented in Figures 8(c) and 8(d) are deformed modes. In particular, the mode with a natural frequency of 3.2 Hz is the bounce mode of the vehicle body (refer to Figure 8(a)), and the mode with a natural frequency of 3.7 Hz is the pitch mode (refer to Figure 8(b)). Conversely, the mode with the natural frequency of 23.8 Hz is the bending mode of the vehicle (refer to Figure 8(c)), and the mode with the natural frequency of 28.4 Hz is the torsional mode (refer to Figure 8(d)). These flexible modes are expected to possess larger natural frequencies than the rigid-body modes.
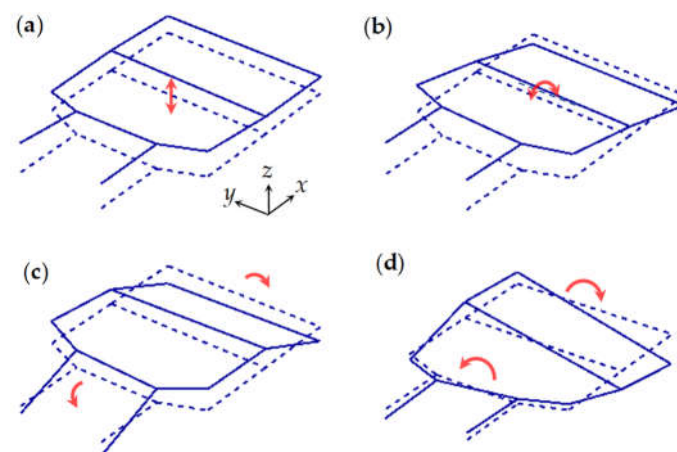


**Figure 8.** Mode shapes of the body floor: (**a**) bounce mode (3.2 Hz); (**b**) pitch mode (3.7 Hz); (**c**) bending mode (23.8 Hz); and (**d**) torsional mode (28.4 Hz).

A comparative study between the ODS and modal test result is crucial for a deeper understanding of the idling vibration produced by the diesel SUV. In general, the ODS of a system is influenced not only by the excitation frequency and direction, but also by the

mode shapes corresponding to the natural frequencies proximate to the excitation frequency. Therefore, the direction of the excitation torque (the engine driving torque) and the mode shapes should be analyzed with respect to the natural frequencies proximate to the idling frequency.

The ODSs at the idling frequency of 27.7 Hz (refer to Figure 5) were compared with the mode shapes (refer to Figures 7 and 8). First, the ODS of the powertrain, as illustrated in Figure 5(a), is almost identical to the pitch mode of the powertrain, as depicted in Figure 7(b). However, the natural frequency of this pitch mode, 13.0 Hz, is significantly different from the idle or excitation frequency, 27.7 Hz. Nevertheless, the powertrain possesses an ODS similar to the shape of the pitch mode because the excitation torque of the engine acts in the transverse direction of the vehicle.

Conversely, the ODS of the radiator (refer to Figure 5(b)) corresponds to the roll mode of the radiator (refer to Figure 7(e)). This roll mode shape was observed in the ODS because the natural frequency of this roll mode, 30.3 Hz, is proximate to the idling frequency, 27.7 Hz. Similarly, the ODS of the intercooler, as depicted in Figure 5(c), resembles the bounce mode of the intercooler, as illustrated in Figure 7(f), featuring a natural frequency of 29.3 Hz, which is proximate to the idling frequency. Finally, the ODS of the body floor displayed in Figure 5(d) appears as a combination of the bending and torsional modes of the body floor, which are respectively depicted in Figures 8(c) and 8(d). These modes contribute to the ODS because the idling frequency (27.7 Hz) lies between the natural frequencies of the bending and torsional modes (23.8 and 28.4 Hz, respectively). Notably, because the excitation torque of the engine is applied to the front-center of the body floor, the bending mode exerts a greater influence on the ODS than the torsional mode.

### 3. Dynamic modeling

On the basis of the experimental analysis reported in the previous section, a dynamic model for the diesel SUV has been established. To analyze the behavior of the low-frequency region below 30 Hz, the dynamic model presented in this study possesses 13 degrees of freedom, as displayed in Figure 9: three degrees of freedom are assigned to the powertrain, two to the radiator, one to the intercooler, and seven to the body floor.
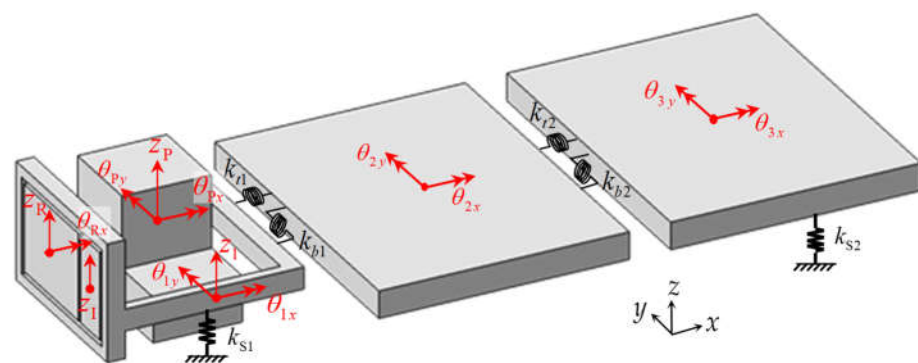


**Figure 9.** Dynamic model of a diesel SUV with 13 degrees of freedom.

First, as shown in Figures 7(a)–7(c), the vibration modes dominating the behavior of the powertrain in the low-frequency region are the bounce, pitch, and roll modes. Accordingly, three degrees of freedom are accorded to the rigid-body motion of the powertrain, and the generalized coordinates for the bounce, pitch, and roll motions are expressed as $z_P$, $\theta_{Py}$, and $\theta_{Px}$, respectively. As depicted in Figures 7(d) and 7(e), the radiator exhibits bounce and roll modes in the low-frequency region; therefore, the generalized coordinates $z_R$ and $\theta_{Rx}$ for the bounce and roll motions are respectively assigned to the radiator. Similarly, the intercooler possesses a bounce mode solely in the low-frequency region (refer to Figure 7(f)); thus, the generalized coordinate $z_I$ for the bounce motion is assigned to the intercooler.

Conversely, the body floor features rigid-body modes such as bounce and pitch modes (refer to Figures 8(a) and 8(b)) as well as flexible modes owing to the bending and torsional deformations (refer to Figures 8(c) and 8(d)) in the low-frequency region. Therefore, both the rigid-body and flexible modes should be considered for the dynamic modeling. Considering these two modes, this study proposes a body floor model comprising three parts: the front, middle, and rear floors, as represented in Figure 9. The motion of the front floor is described with the generalized coordinates for the bounce, pitch, and roll motions (respectively denoted by $z_1$, $\theta_{1y}$, and $\theta_{1x}$), the motion of the middle floor is described with the coordinates for the pitch and roll motions (respectively denoted by $\theta_{2y}$ and $\theta_{2x}$), and the motion of the rear floor is described with the coordinates for pitch and roll motions (respectively denoted by $\theta_{3y}$ and $\theta_{3x}$). Degrees of freedom were not imposed on the bounce motions of the middle and rear floors because the midpoint of the interface between the front and middle floors and the midpoint of the interface between the middle and rear floors were assumed to be constrained by revolute joints.

The inertia properties, such as masses and mass moments of inertia, are required to construct the dynamic model of the SUV. The masses of relatively small components such as the radiator, intercooler, and powertrain were measured using a scale. However, masses and mass moments of inertia, which are difficult to measure, were analytically extracted using three-dimensional solid computer-aided design models. On the basis of the nodal lines of bending and torsional deformations obtained from the ODS analysis, the body floor was categorized into three segments: the front, middle, and rear floors. The inertia properties used in the dynamic model are summarized in Table 1.

**Table 1.** Inertia properties used to construct the dynamic model.

| Component | Mass (kg) | Mass moment of inertia (kg·m²) | | | | | |
|---|---|---|---|---|---|---|---|
| | m | $I_x$ | $I_y$ | $I_z$ | $I_{xy}$ | $I_{yz}$ | $I_{zx}$ |
| Powertrain | 301.4 | 11.55 | 24.01 | 23.14 | 1.49 | 0.04 | -4.45 |
| Radiator | 11.5 | 0.57 | 0.33 | 0.52 | 0 | 0 | 0 |
| Intercooler | 5.0 | 0.13 | 0.12 | 0.02 | 0 | 0 | 0 |
| Front floor | 523.5 | 119.45 | 113.37 | 171.94 | -0.59 | 1.21 | -9.43 |
| Middle floor | 426.1 | 148.26 | 81.02 | 131.76 | -0.39 | 0.10 | -0.96 |
| Rear floor | 474.3 | 115.50 | 120.27 | 134.17 | 0.58 | -0.45 | -1.50 |

In addition, to establish the dynamic model, the stiffness and damping properties related to the radiator, intercooler, powertrain, and floors should be evaluated. As discussed earlier, the radiator is connected to the front floor via four rubber bushings, and the intercooler is connected to the front floor via three rubber bushings. The radiator and the intercooler are each connected to the powertrain through two rubber hoses. Moreover, the powertrain is supported at three positions by the engine, transmission, and roll mounts. The equivalent springs and dampers of these mounts, bushings and hoses are displayed in Figure 10. The equivalent stiffness and damping coefficient of the radiator rubber bushing are respectively denoted by $k_R$ and $c_R$, and the stiffness and damping coefficient of the intercooler rubber bushing are respectively represented by $k_I$ and $c_I$. The upper radiator hose exhibits a stiffness of $k_{H1}$ and damping coefficient of $c_{H1}$, whereas the lower radiator hose possesses a stiffness of $k_{H2}$ and damping coefficient of $c_{H2}$. Similarly, the upper intercooler hose demonstrates a stiffness of $k_{H3}$ and damping coefficient $c_{H3}$, whereas the lower intercooler hose exhibits a stiffness of $k_{H4}$ and damping coefficient of $c_{H4}$. Finally, the stiffness and damping coefficient are respectively denoted by $k_{P1}$ and $c_{P1}$ for the engine mount, by $k_{P2}$ and $c_{P2}$ for the transmission mount, and by $k_{P3}$ and $c_{P3}$ for the roll mount.
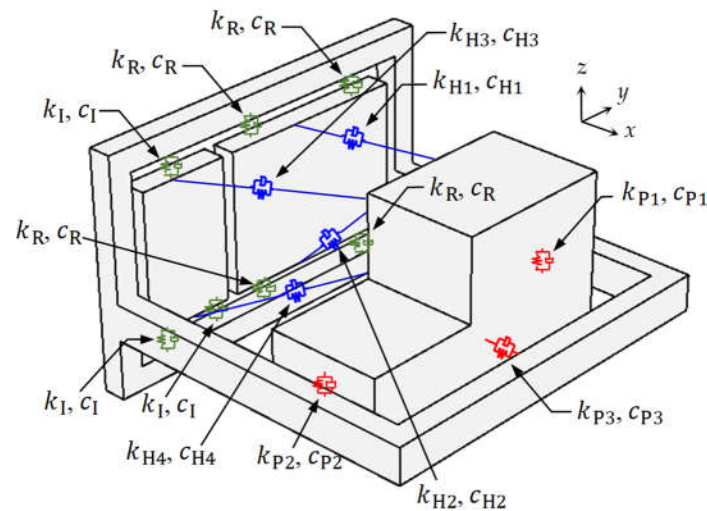
**Figure 10.** Equivalent stiffnesses and damping coefficients between the powertrain, radiator, inter-cooler, and front floor.

The equivalent stiffnesses and damping coefficients of the mounts, bushings, and hoses were obtained from the experiments by using the measurement setup illustrated in Figure 11(a). Under the given condition that the mount, bushing, or hose, which is the test object, was placed between the mass block and the rigid wall, the mass was excited with a shaker at the idling frequency. As shown in this figure, the excitation force and displacement of the mass were measured with a force transducer and a gap sensor, respectively. The equation of motion for the physical model of the measurement setup, which is illustrated in Figure 11(b), can be expressed as

$$m\ddot{x} + c\dot{x} + kx = Fe^{j\omega t} \tag{1}$$

where the superposed dot represents differentiation with respect to time, $x$ denotes the displacement of the mass; $m$ represents the mass of the block (0.5 kg), $c$ and $k$ respectively symbolize the damping coefficient and stiffness of the specimen, and $F$ and $\omega$ denote the amplitude and frequency of the excitation force, respectively.
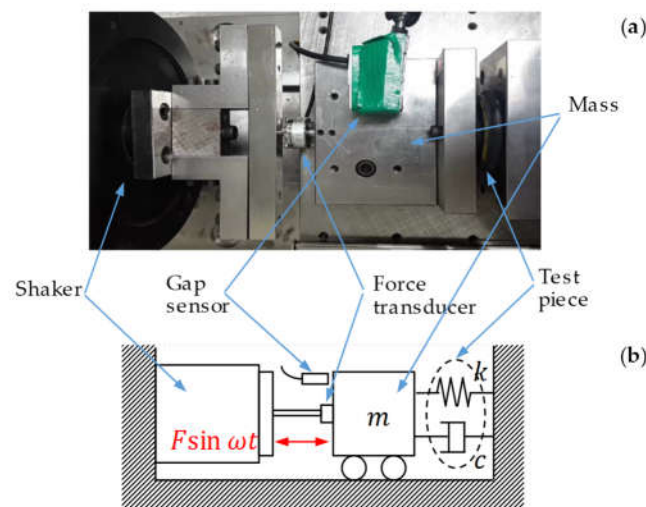


**Figure 11.** Measurement setup of the stiffnesses and damping coefficients for mounts, rubber bushings, and hoses: (**a**) the photo of actual device and (**b**) the corresponding physical model.

Upon assuming $x = Xe^{j\omega t}$, the dynamic stiffness, defined as the ratio of the excitation force and the displacement, is expressed as follows:

$$F/X = k - m\omega^2 + \mathrm{j}\omega c \tag{2}$$

Considering the real and imaginary parts of the experimentally obtained dynamic stiffness, which are denoted by $k_r$ and $k_i$, respectively, the stiffness and damping coefficient for the specimen can be obtained as follows:

$$k = k_r + m\omega^2, \quad c = k_i/\omega \tag{3}$$

The excitation frequency, $\omega$, was selected as the idling frequency of 27.7 Hz. The dynamic stiffness for the rubber bushing of the radiator is presented in Figure 12, wherein Figures 12(a) and 12(b) correspond to the real and imaginary parts of the dynamic stiffness, respectively. In this figure, the real and imaginary parts at the idling frequency of 27.7 Hz are respectively denoted by $k_r = 38.2$ N/mm and $k_i = 10.0$ N/mm. By substituting these values into Equation (3), the equivalent stiffness and damping are respectively calculated as $k = 53.3$ N/mm and $c = 57.5$ kg/s. Similarly, the stiffnesses and damping coefficients of bushings and hoses obtained through experiments are summarized in Table 2.
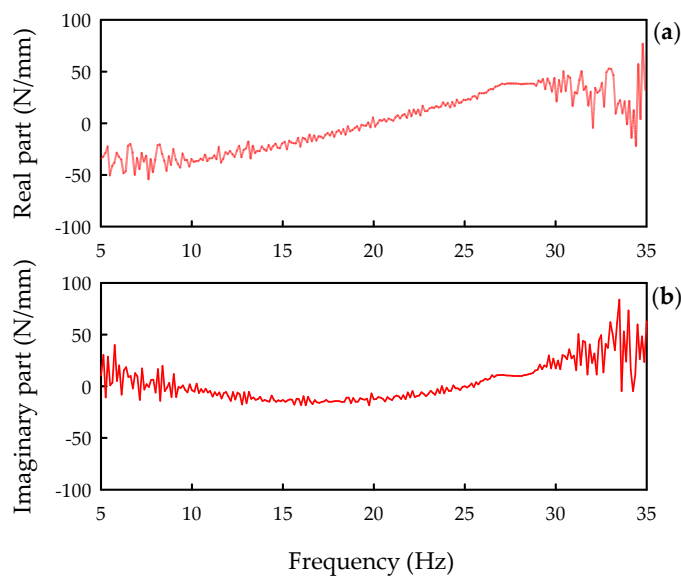


**Figure 12.** Dynamic stiffness for the rubber bushing of the radiator: (**a**) the real part and (**b**) the imaginary part.

**Table 2.** Equivalent stiffnesses and damping coefficients of the bushings, hoses, and mounts at the idle frequency of 27.7 Hz.

| Component | Part | Stiffness (N/mm) | Damping coefficient (kg/s) |
|---|---|---|---|
| | Rubber bushing | 53.3 | 57.5 |
| Radiator | Upper hose | 5.0 | 157.7 |
| | Lower hose | 12.8 | 88.9 |
| | Rubber bushing | 55.2 | 54.4 |
| Intercooler | Upper hose | 10.2 | 150.3 |
| | Lower hose | 13.6 | 189.8 |
| | Engine mount | 500.2 | 1223.8 |
| Powertrain | Transmission mount | 497.5 | 375.1 |
| | Roll mount | 2911.6 | 2553.4 |

After independently obtaining the tire stiffness and suspension stiffness, these stiffnesses, which were assumed to be connected in series, were used to derive the equivalent stiffness of the tire and suspension combination. The tire stiffness was measured as per

the static load-deflection test proposed by Taylor et al. [22]. The static load–deflection test determines the vertical load of a tire by measuring the vertical deflection under a vertical load from a regression curve that represents the load as a function of displacement, after which the function is differentiated with the displacement. In the static load-deflection test, the vertical deflection of a tire is measured by varying the vertical load. After expressing the load as a function of deflection, the tire stiffness is obtained by differentiating this function by the deflection at a specific deflection value. Moreover, using the suspension kinematics and compliance test system [23], the vertical stiffness of the vehicle suspension was determined by measuring the vertical deflection under the applied vertical load. The equivalent vertical stiffnesses of the front and rear suspension/tire combinations obtained from these methods are 28.9 and 31.6 N/mm, respectively.

The equivalent bending and torsional stiffnesses between the front, middle, and rear body floors were obtained using a commercial package for finite element analysis. The process of obtaining equivalent stiffness between the front and middle body floors are described herein. As shown in Figure 13, the front body floor was discretized into finite elements with the commercial package, and the middle and rear floors were modeled as stationary rigid bodies. The boundary between the front and middle body floors was considered to be fixed. The load conditions for obtaining the equivalent bending and torsional stiffnesses between the front and middle floors are displayed in Figures 13(a) and 13(b), respectively. To determine the bending stiffness, as shown in Figure 13(a), uniform vertical forces of $F = 10$ N were applied to both ends of the front-end module in the same direction. In addition, to determine the torsional stiffness, as illustrated in Figure 13(b), vertical forces in opposite directions were applied at both ends. The deflections at the front corner of the front-end module for the load conditions, which are depicted in Figures 13(a) and 13(b), obtained from the finite element analysis are 5.7 and 0.85 mm, respectively.
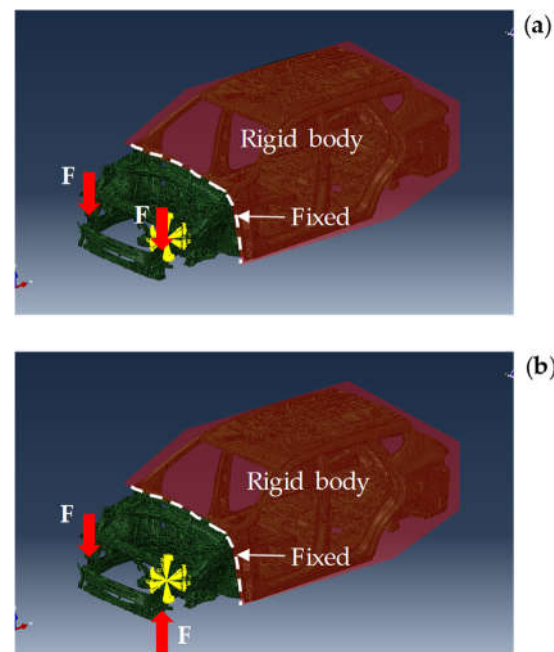


**Figure 13.** Finite element models to obtain equivalent stiffnesses between the front and middle body floors: (**a**) the load condition for the bending stiffness and (**b**) the load condition for the torsional stiffness.

To determine the equivalent stiffnesses, the rigid front body floor illustrated in Figure 9 has been schematically redrawn in Figure 14, wherein Figure 14(a) features the side view of the SUV, and its front view is displayed in Figure 14(b). As depicted in this figure, the force, $F$, is the same force of 10 N that was imposed in the finite element analysis, and $l_1$ and $w_1$ denote the length of the front floor (907 mm) and the half-width of the vehicle

(428.5 mm), respectively. In Figure 14, $k_{b1}$ and $k_{t1}$ respectively symbolize the bending and torsional stiffnesses between the front and middle floors, which are identical to those represented in Figure 9, and $\delta_{1b}$ and $\delta_{1t}$ respectively denote the bending and torsional deflections. From the free-body diagrams in Figure 14, the bending and torsional stiffnesses are obtained as

$$k_{b1} = 2Fl_1^2/\delta_{1b}, \quad k_{t1} = 2Fw_1^2/\delta_{1t} \tag{4}$$

Substituting the bending and torsion deflections of $\delta_{1b} = 5.7$ mm and $\delta_{1t} = 0.85$ mm, which were obtained from the finite element analysis, into Equation (4), the bending and torsional stiffnesses between the front and middle floors were calculated as $2.886 \times 10^6$ and $4.320 \times 10^6$ N/mm, respectively. Similarly, the bending and torsional stiffnesses between the middle and rear body floors were determined as $3.584 \times 10^6$ and $2.917 \times 10^6$ N/mm.
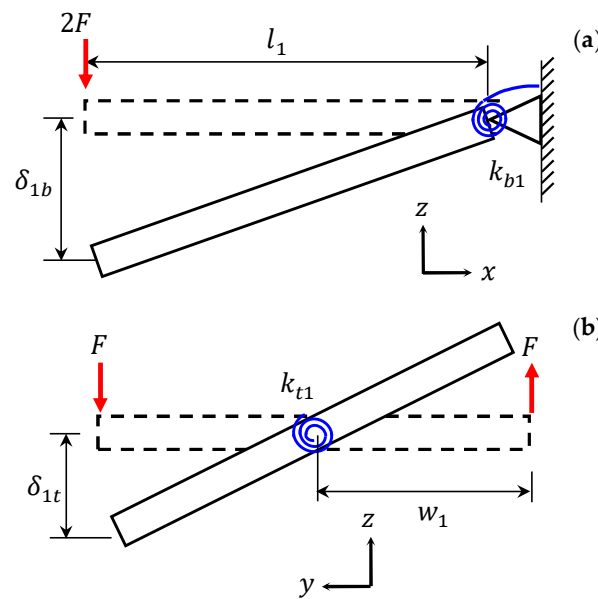


**Figure 14.** Rigid model of the front body floor to obtain equivalent stiffnesses between the front and middle body floors: (**a**) the bending stiffness and (**b**) the torsional stiffness.

Subsequently, the excitation forces and moments generated from the engine in the powertrain were analyzed. These excitations are induced by the gas pressure resulting from the explosion inside the cylinder as well as the unbalanced inertia force owing to the piston, connecting rod, and crank. Generally, the primary and secondary inertia forces of the engine are negated by the crank and the balance shaft. Furthermore, the excitation forces and the pitch excitation moment are relatively low compared to the roll excitation moment. Therefore, in this study, the roll excitation moment generated by the gas pressure was considered as the main excitation force in the idle state. Considering the explosion mechanism in a cylinder, the piston, connecting rod and crank are illustrated in Figure 15, wherein $P$ denotes the gas pressure, $l$ represents the length of the connecting rod, $r$ depicts the length of the crank arm, and $\omega$ symbolizes the angular velocity of the crankshaft. The gas torque, $M$, owing to the gas pressure at time $t$ is expressed as follows [24]:

$$M = PAr\left(\sin \omega t + \frac{r}{2l}\sin 2\omega t\right) \tag{5}$$

where $A$ denotes the piston area. In case of the four-cylinder diesel engine considered for this study, because the explosions occur with phase differences of 180 degrees in the two pairs of cylinders, the total gas torque, $M_t$, generated by the four cylinders is expressed as follows:

$$M_t = \frac{2PAr^2}{l} \sin 2\omega t \qquad (6)$$

The diesel SUV employed in this study possessed a gas pressure of $P = 9.45$ N/mm², connecting rod length of $l = 145$ mm, crank arm length of $r = 48$ mm, and piston area of $A = 5728$ mm². By substituting these values into Equation (6), the magnitude of the total moment was computed as $1.72 \times 10^6$ Nmm from Eq. (6). For the idling frequency of 27.7 Hz, the angular frequency, $2\omega$, is calculated as 348.09 rad/s. However, as reported in a study, only 1–5% of the total gas torque generally contributes to the vibration excitation torque [25]. Considering the low engine speed and its stable idle state, 1% of the gas torque presumably contributed to the excitation torque. Therefore, when the engine is in the idle state, the amplitude of the roll excitation moment finally applied to the dynamic model was $1.72 \times 10^4$ Nmm.
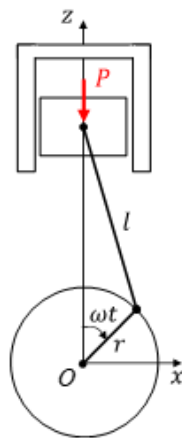


**Figure 15.** Schematic diagram of an engine crank mechanism.

## 4. Derivation of the equations of motion

As detailed in this section, the equations of motion for the dynamic model, which were proposed in the previous section, were derived and verified. The equations of motion were derived using Lagrange equations with constraints, which are expressed as follows:

$$\frac{\mathrm{d}}{\mathrm{d}t}\left(\frac{\partial T}{\partial \dot{q}_k}\right) + \frac{\partial F_d}{\partial \dot{q}_k} - \frac{\partial T}{\partial q_k} + \frac{\partial V}{\partial q_k} + \sum_{l=1}^{6} \lambda_l \frac{\partial g_l}{\partial q_k} = f_k \qquad (7)$$

where $q_k$ $(k = 1, 2, \cdots, 19)$ represent 19 coordinates describing the motions of the dynamic model: $z_P$, $\theta_{Px}$, $\theta_{Py}$, $z_R$, $\theta_{Rx}$, $z_I$, $z_1$, $\theta_{1x}$, $\theta_{1y}$, $x_2$, $y_2$, $z_2$, $\theta_{2x}$, $\theta_{2y}$, $x_3$, $y_3$, $z_3$, $\theta_{3x}$, and $\theta_{3y}$. In the aforementioned equation, $T$, $V$, and $F_d$ denote the kinetic energy, potential energy, and Rayleigh's dissipation function, respectively, $f_k$ symbolizes the generalized nonconservative forces, $g_l$ represent the constraints, and $\lambda_l$ depict the Lagrange multipliers. Notably, the coordinates presented herein include 6 coordinates of $x_2$, $y_2$, $z_2$, $x_3$, $y_3$, and $z_3$ in addition to the 13 independent generalized coordinates mentioned in Section 3. To express the kinetic and potential energies more effectively in terms of the coordinates, the additional 6 coordinates were introduced. The constraints related to the additional coordinates are discussed herein.

First, consider the kinetic energy of the dynamic model for the diesel SUV, which can be expressed as

$$T = \frac{1}{2}\sum m_i \mathbf{v}_i^{\mathrm{T}} \mathbf{v}_i + \frac{1}{2}\sum \boldsymbol{\omega}_i^{\mathrm{T}} \mathbf{I}_i \boldsymbol{\omega}_i \qquad (8)$$

where $i$ represents the six parts of the SUV: the powertrain, radiator, intercooler, front floor, middle floor, and rear floor, $m_i$ indicate the masses of these parts, $\mathbf{v}_i$ represents the velocity vectors of the mass centers, $\omega_i$ denotes the angular velocity vectors, and $\mathbf{I}_i$ symbolizes the inertia matrices about the mass centers. The first term in the right-hand side of the equation represents the translational kinetic energy, whereas the second term is for the rotational kinetic energy. The velocity vector of mass center and angular velocity vectors for each part were defined in the global coordinate system. The kinetic energy was determined by substituting the velocity and angular velocity vectors and the inertia properties of Table 1 into Equation (8).

The potential energy and Rayleigh's dissipation function owing to the stiffness and damping properties of the mounts, bushings, hoses, and body floor connections are expressed as

$$V = \frac{1}{2}\sum k_j\left(\Delta l_j\right)^2 + \frac{1}{2}\sum k_r(\Delta\theta_r)^2 \tag{9}$$

$$F_d = \frac{1}{2}\sum c_s(\Delta v_s)^2 \tag{10}$$

where subscript $j$, $r$ represent the equivalent translational and rotational springs, respectively, $k_j$ and $k_r$ are the equivalent translational and rotational stiffnesses, respectively. Subscript $s$ represent the equivalent translational dampers, $c_s$ are the equivalent damping coefficients. $\Delta l_j$ are the stretches of the equivalent translational springs, $\Delta\theta_r$ are the angular changes of the equivalent torsional springs, and $\Delta v_s$ are the velocity changes in the equivalent dampers. By expressing $\Delta l_j$, $\Delta\theta_r$ and $\Delta v_s$ in terms of the 19 coordinates and substituting the equivalent stiffnesses and damping coefficients, which are listed in Table 2, and the equivalent stiffnesses of floor connections into Equations (9) and (10), the potential energy and Rayleigh's dissipation function were expressed with these coordinates. Because the kinetic energy, potential energy, and Raleigh's dissipation function expressed in terms of the 19 coordinates are extremely complex, these expressions have been excluded from this paper. Because the total gas torque expressed in Equation (6) is the sole load applied to the system, the generalized forces can be represented as

$$f_3 = M_t \text{ and } f_k = 0 \text{ for } k \neq 3 \tag{11}$$

The constraints between the front, middle, and rear body floors were analyzed. As discussed earlier, the 19 coordinates are not independent of each other and only 13 coordinates are independent; thus, the proposed dynamic model features 6 constraints. These constraints are illustrated in Figure 16, wherein $C_1$ and $C_2$ symbolize the contact points of the front and middle floors and the middle and rear floors, respectively, $G_1$, $G_2$ and $G_3$ denote the mass centers of the front, middle and rear floors; $\mathbf{r}_1, \mathbf{r}_2$ and $\mathbf{r}_3$ represent the position vectors from the reference point $O$ to the points $G_1$, $G_2$ and $G_3$, $\mathbf{s}_{12}$ denotes a vector from point $G_1$ to point $C_1$; $\mathbf{s}_{21}$ and $\mathbf{s}_{22}$ depict vectors from point $G_2$ to points $C_1$ and $C_2$, respectively, and $\mathbf{s}_{32}$ represents a vector from point $G_3$ to point $C_2$. In this study, the following constraints were implemented in the dynamic model: the interface midpoints of the front and middle floors are connected, and the interface midpoints of the middle and rear floors are connected. In addition, the floors notably exhibit the roll and pitch motions (rotations about the x- and y-axes) without the yaw motion (rotation about the z-axis). Under these conditions, the constraint in which the interface midpoints of the front and middle floors are connected can be expressed as

$$\mathbf{g}_{12} = \mathbf{r}_1 + \mathbf{T}_1\mathbf{s}_{12} - \mathbf{r}_2 - \mathbf{T}_2\mathbf{s}_{21} = \mathbf{0} \tag{12}$$

and the constraint in which the interface midpoints of the middle and rear floors are connected can be expressed as

$$\mathbf{g}_{23} = \mathbf{r}_2 + \mathbf{T}_2\mathbf{s}_{22} - \mathbf{r}_3 - \mathbf{T}_3\mathbf{s}_{32} = \mathbf{0} \tag{13}$$

In Equations (12) and (13), the constraint vectors are expressed as

$$\mathbf{g}_{12} = \{g_1, g_2, g_3\}^{\mathrm{T}}, \quad \mathbf{g}_{23} = \{g_4, g_5, g_6\}^{\mathrm{T}} \tag{14}$$

and the rotation matrices are expressed as

$$\mathbf{T}_n = \begin{bmatrix} 1 & 0 & 0 \\ 0 & \cos\theta_{nx} & -\sin\theta_{nx} \\ 0 & \sin\theta_{nx} & \cos\theta_{nx} \end{bmatrix} \begin{bmatrix} \cos\theta_{ny} & 0 & \sin\theta_{ny} \\ 0 & 1 & 0 \\ -\sin\theta_{ny} & 0 & \cos\theta_{ny} \end{bmatrix} \text{ for } n = 1, 2, 3 \tag{15}$$

The constraints for this dynamic model are represented by

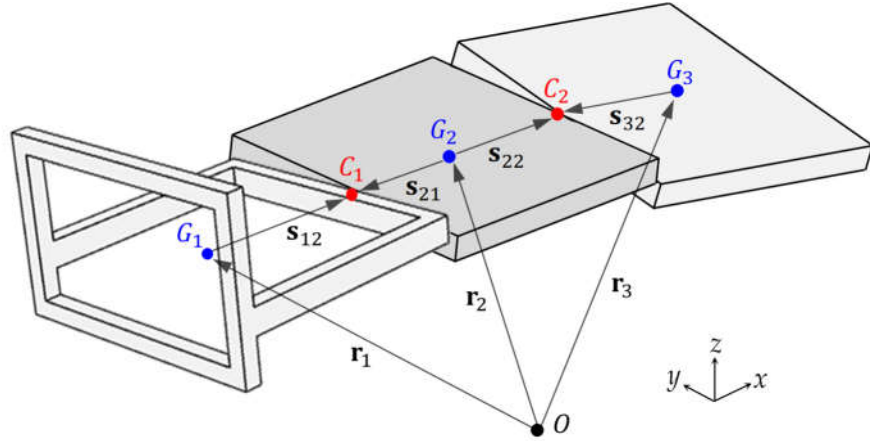$$g_l(q_1, q_2, \cdots, q_{19}, t) = 0 \ \text{ for } \ l = 1, 2, \cdots, 6 \tag{16}$$



**Figure 16.** Constraints between the front, middle, and rear body floors.

Upon substitution of the kinetic energy, potential energy, Raleigh's dissipation function, generalized forces, and the constraints into the Lagrange equations, the equations of motion and the constraints can be derived as follows:

$$\mathbf{M}\ddot{\mathbf{q}} + \mathbf{N}(\mathbf{q}, \dot{\mathbf{q}}) + \mathbf{A}^{\mathrm{T}}\boldsymbol{\lambda} = \mathbf{f} \tag{17}$$

$$\mathbf{g} = \mathbf{0} \tag{18}$$

where $\mathbf{M}$ denotes the mass matrix, $\mathbf{N}$ represents the nonlinear internal force vector, $\mathbf{q}$ symbolizes the displacement vector, $\mathbf{f}$ depicts the applied load vector, $\boldsymbol{\lambda}$ depicts the Lagrange multiplier vector, $\mathbf{g}$ represents the constraint vector, and $\mathbf{A}$ denotes the Jacobian matrix. $\mathbf{g}$ can be also expressed as $\mathbf{g} = \mathbf{Aq}.$

$$\mathbf{q} = \{z_P, \theta_{Px}, \theta_{Py}, z_R, \theta_{Rx}, z_I, z_1, \theta_{1x}, \theta_{1y}, x_2, y_2, z_2, \theta_{2x}, \theta_{2y}, x_3, y_3, z_3, \theta_{3x}, \theta_{3y}\}^{\mathrm{T}} \tag{19}$$

$$\mathbf{f} = \{0, 0, M_t, 0, 0, 0, 0, 0, 0, 0, 0, 0, 0, 0, 0, 0, 0, 0, 0\}^{\mathrm{T}} \tag{20}$$

$$\boldsymbol{\lambda} = \{\lambda_1, \lambda_2, \lambda_3, \lambda_4, \lambda_5, \lambda_6\}^{\mathrm{T}}, \ \mathbf{g} = \{g_1, g_2, g_3, g_4, g_5, g_6\}^{\mathrm{T}} \tag{21}$$

$$\mathbf{A} = \frac{\mathrm{d}\mathbf{g}}{\mathrm{d}\mathbf{q}} \tag{22}$$

By differentiating Equation (18) twice with respect to time, the following equation is obtained:

$$\mathbf{A}\ddot{\mathbf{q}} = -\dot{\mathbf{A}}\dot{\mathbf{q}} \tag{23}$$

All the displacements are assumed to be minimal because $\mathbf{N}(\mathbf{q}, \dot{\mathbf{q}})$ is linearized as $\mathbf{C}\dot{\mathbf{q}} + \mathbf{Kq}$, where $\mathbf{C}$ is the damping matrix and $\mathbf{K}$ is the stiffness matrix. In this case, the nonlinear

equations of motion expressed in Equation (17) can be reduced to the following linearized matrix–vector equation:

$$\mathbf{M\ddot{q}} + \mathbf{C\dot{q}} + \mathbf{Kq} + \mathbf{A}_L^T\boldsymbol{\lambda} = \mathbf{f} \tag{24}$$

where $\mathbf{A}_L$ denotes the linearized Jacobian matrix. The linearized version of Equation (23) is expressed as

$$\mathbf{A}_L\mathbf{\ddot{q}} = \mathbf{0} \tag{25}$$

Notably, $\mathbf{M}$, C, and $\mathbf{K}$ are $19 \times 19$ matrices, and $\mathbf{A}_L$ is a $6 \times 19$ matrix.

The linearized equations of motion were verified by comparing the analytically computed natural frequencies with the experimentally measured natural frequencies. Because the damping of the system does not have a significant effect on the computation of the natural frequencies, the damping term, $\mathbf{C\dot{q}}$, and the applied load, $\mathbf{f}$ were neglected in the computations of the natural frequencies using the model presented in this study. For $\mathbf{q} = \mathbf{Q}e^{i\omega t}$ and $\boldsymbol{\lambda} = \boldsymbol{\Lambda}e^{i\omega t}$, where $i = \sqrt{-1}$, the natural frequencies for the equations of motion with constraints were derived from the following eigenvalue problem [26]:

$$\begin{bmatrix} \mathbf{K} & \mathbf{A}_L^T \\ \mathbf{A}_L & \mathbf{0} \end{bmatrix} \begin{Bmatrix} \mathbf{Q} \\ \boldsymbol{\Lambda} \end{Bmatrix} = \omega^2 \begin{bmatrix} \mathbf{M} & \mathbf{0} \\ \mathbf{0} & \mathbf{0} \end{bmatrix} \begin{Bmatrix} \mathbf{Q} \\ \boldsymbol{\Lambda} \end{Bmatrix} \tag{26}$$

Equation (26) equation yields the characteristic equation expressed as

$$\det[\mathbf{A}_L(\mathbf{K} - \omega^2\mathbf{M})^{-1}\mathbf{A}_L^T] = 0 \tag{27}$$

In Table 3, the natural frequencies, which are computed from Equation (25) using the properties detailed in Section 3, are compared with the natural frequencies obtained from the modal tests, as reported in Section 2. According to the information listed in this table, the analytically calculated natural frequencies are in agreement with the experimentally measured frequencies.

**Table 3.** Comparison of the natural frequencies obtained by simulation and experiment.

| Component | Mode | Natural frequency (Hz) | | |
| --- | --- | --- | --- | --- |
| | | Simulation | Experiment | Difference |
| Powertrain | Bounce mode | 6.7 | 4.8 | –1.9 |
| | Pitch mode | 15.3 | 13.0 | –2.3 |
| | Roll mode | 21.1 | 18.5 | –2.6 |
| Radiator | Bounce mode | 19.4 | 20.0 | 0.6 |
| | Roll mode | 30.3 | 30.3 | 0.0 |
| Intercooler | Bounce mode | 31.0 | 29.3 | -1.7 |
| Body floor | Bounce mode | 1.2 | 3.2 | 2 |
| | Pitch mode | 1.7 | 3.7 | 2 |
| | Bending mode | 25.2 | 23.8 | –1.4 |
| | Torsional mode | 28.0 | 28.4 | 0.4 |

Subsequently, the mass effects of the radiator and intercooler on the vibration level during engine idling were investigated through a simulation and an experiment, and the proposed dynamic model was verified again by demonstrating that the mass effects exhibit identical tendencies in the simulation as well as the experiment. Prior to verification, the simulation process was considered to obtain the frequency response function for the constrained system, which is defined in Equations (24) and (25). Let the displacement and Lagrange multiplier vectors be $\mathbf{q} = \mathbf{Q}e^{i\omega t}$ and $\boldsymbol{\lambda} = \boldsymbol{\Lambda}e^{i\omega t}$, , and let the applied load be $\mathbf{f} = \mathbf{F}e^{i\omega t}$; thus, Equations (24) and (25) can be rewritten as follows:

$$\mathbf{H}(\omega)^{-1}\mathbf{Q} + \mathbf{A}_L^T\boldsymbol{\Lambda} = \mathbf{F} \tag{28}$$

$$\mathbf{A}_L\mathbf{Q} = \mathbf{0} \tag{29}$$

where $\mathbf{H}(\omega) = (\mathbf{K} - \omega^2\mathbf{M} + i\omega\mathbf{C})^{-1}$. From Equations (28) and (29), the displacement response vector $\mathbf{Q}$ can be expressed as $\mathbf{Q} = \widehat{\mathbf{H}}(\omega)\mathbf{F}$, where $\widehat{\mathbf{H}}(\omega)$ is the frequency response function for constrained system expressed as follows.

$$\widehat{\mathbf{H}}(\omega) = \mathbf{H}(\omega)\{\mathbf{I} - \mathbf{A}_L^T[\mathbf{A}_L\mathbf{H}(\omega)\mathbf{A}_L^T]^{-1}\mathbf{A}_L\mathbf{H}(\omega)\} \tag{30}$$
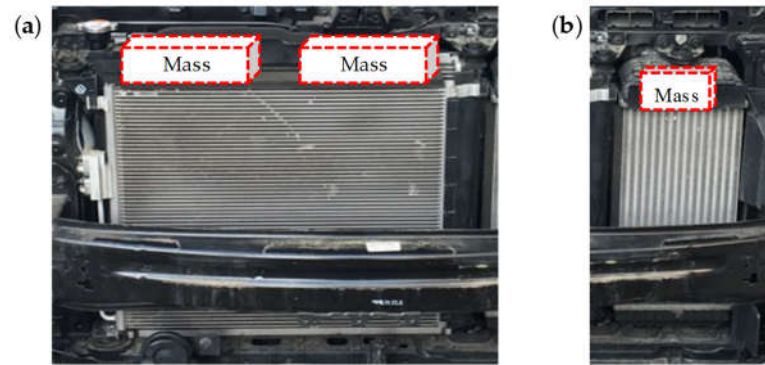


**Figure 17.** Schematics of added masses to analyze the effect of radiator or intercooler mass on vibration level: (**a**) the radiator and (**b**) the intercooler.
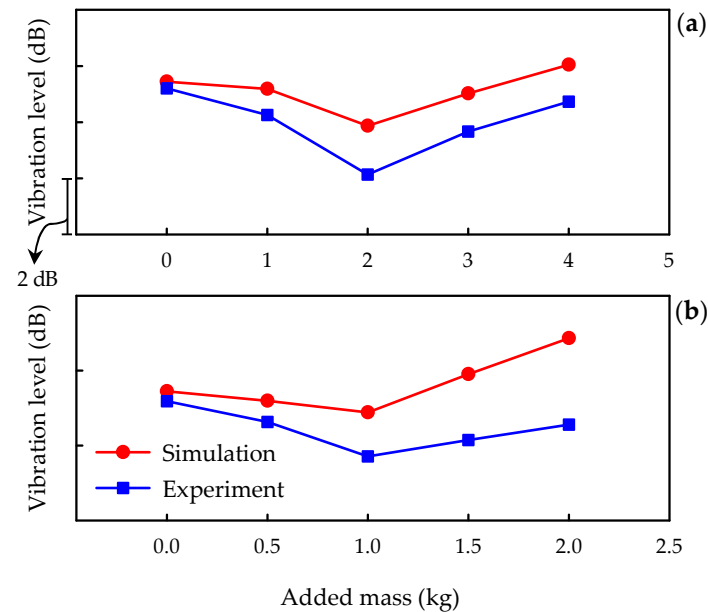


**Figure 18.** Comparison of vibration levels between the simulation and experiment obtained by changing the amount of added mass: (**a**) the radiator and (**b**) the intercooler.

The vibration levels were experimentally measured in the idle engine state by adding mass blocks of various sizes to the radiator or intercooler as illustrated in Figure 17. The added masses were 1, 2, 3, and 4 kg for the radiator and 0.5, 1.0, 1.5, and 2.0 kg for the intercooler. The vibration levels were measured at the driver's seat position on the body floor at an engine speed of 830 rpm, i.e., an idling frequency of 27.7 Hz. In addition, using the added blocks in the experiments for the radiator and intercooler, simulations were performed with the dynamic model established in this study. The vibration levels obtained through simulation and experiment for changes in the added mass are listed in Figure 18 for a comparative study. Although the vibration levels of the simulation and the experiment are slightly different, the trends of the overall increasing and decreasing levels are notably similar. As described earlier, the dynamic model established in this study was

verified by comparing the natural frequencies and vibration levels obtained from the simulation and experiment.

### 5. Design optimization for the idle vibration reduction

The design was optimized using the verified dynamic model to reduce the vibration during engine idling. To formulate the optimal design, the vibration level during engine idling at the position of the driver's seat on the body floor was selected as an objective function, and the physical properties related to the radiator and intercooler were regarded as the design variables. Prior to design optimization, the effects of the design variables on the vibration level on the driver's seat were analyzed. Using these variables, the design was optimized to minimize the vibration during the idle engine state. According to the results, the idling vibration level obtained from the optimal design was reduced compared to the level of the present design. Furthermore, the mechanism for reducing the vibration in the idle engine state was analyzed, and a design guideline to reduce the vibration was suggested.

The design variables considered in the design optimization stage to minimize the vibration level during engine idling comprise the masses of the radiator and intercooler, the stiffnesses of the rubber bushings, and the stiffnesses of the hoses. These attributes were selected as the design variables because they facilitate design changes without the requirement of considerable structural changes to the vehicle. The present values and the lower and upper limits of the design variables are listed in Table 4. The lower and upper design limits for the masses of the radiator and intercooler were set to 80% and 120% of the present values, respectively. Conversely, the lower design limits for the stiffnesses of the rubber bushings and hoses were selected as 50% of the present values, and the upper limits were selected as 200% of the present value. Compared to substantially changing the masses of the radiator and intercooler, which is a challenging task, changing the stiffnesses of the bushings and hoses is relatively feasible; thus the aforementioned lower and upper limits were selected. Moreover, considering that the enhancement of the stiffnesses of the bushings and hoses is more convenient to execute than their reduction, their lower and upper limits were set to 50 and 200% of the present values.

**Table 4.** Present values, the lower and upper limits, and optimized values of the design variables.

| Component | Design variables | Present value | Lower limit | Upper limit | Optimized value |
|---|---|---|---|---|---|
| Radiator | Mass (kg) | 11.5 | 9.2 | 13.8 | 11.2 |
| | Stiffness of the rubber bushing (N/mm) | 53.3 | 26.7 | 106.6 | 106.6 |
| | Stiffness of the upper hose (N/mm) | 57.1 | 28.6 | 114.2 | 54.8 |
| | Stiffness of the lower hose (N/mm) | 79.9 | 40.0 | 159.8 | 40.0 |
| Intercooler | Mass (kg) | 5.0 | 4.0 | 6.0 | 6.0 |
| | Stiffness of the rubber bushing (N/mm) | 98.1 | 49.1 | 196.2 | 102.2 |
| | Stiffness of the upper hose (N/mm) | 65.5 | 32.8 | 131.0 | 32.8 |
| | Stiffness of the lower hose (N/mm) | 63.0 | 31.5 | 126.0 | 31.5 |

A parametric study was conducted to investigate the influence of the aforementioned design variables on the objective function, i.e., the vibration level on the driver's seat during engine idling. The variations in value of the objective function were observed while altering a design variable value between the lower and upper limits for all variables, excluding the corresponding variable, set at their present values. The results of the parametric study for the eight design variables, which are listed in Table 4, are illustrated in Figure 19. All the variables are normalized with respect to their present values indicated by the subscript "0"; the changes in the idle vibration level are displayed for the normalized values from 0.5 to 1.5. As depicted in the figure, the idle vibration level is considerably affected by the radiator mass (refer to Figure 19 (a)), the intercooler mass (refer to Figure

19(b)), the rubber bushing stiffness of the radiator (refer to Figure 19 (c)), and the lower hose stiffness of the intercooler (Figure 19(h)). However, the idle vibrations are relatively less affected by the rubber bushing stiffness of the intercooler (refer to Figure 19(d)), the upper hose stiffness of the radiator (Figure 19(e)), the lower hose stiffness of the radiator (Figure 19(f)), and the upper hose stiffness of the intercooler (Figure 19(g)).
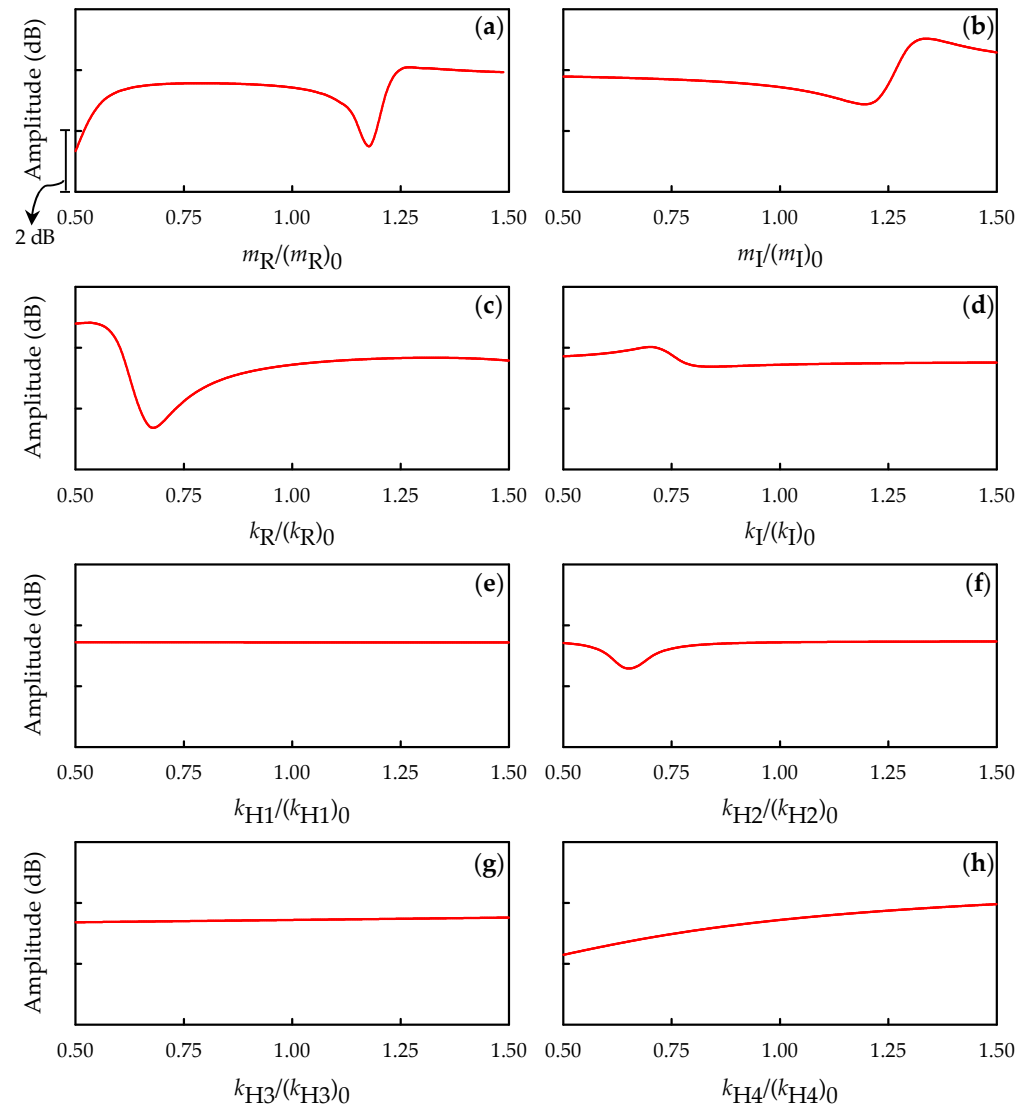


**Figure 19.** Idle vibration levels for the variations of the eight design variables: (**a**) radiator mass; (**b**) intercooler mass; (**c**) rubber bushing stiffness of the radiator; (**d**) rubber bushing stiffness of the intercooler; (**e**) upper hose stiffness of the radiator; (**f**) lower hose stiffness of the radiator; (**g**) upper hose stiffness of the intercooler; and (**h**) lower hose stiffness of the intercooler.

The sensitivities of the design variables were analyzed to determine the variables that considerably influence the idle vibration. To perform the sensitivity analysis, an established experimental design was adopted, which can extract the maximum information for a minimal number of experiments. For the experimental design, the idle vibration level was selected as the objective function along with the aforementioned eight design variables, and the variables were set in three levels: the lower limit, present value, and upper limit. The incorporation of levels is advantageous because a greater number of levels will yield more accurate results; however, this method significantly increases the experimental time and cost involved. Accordingly, three levels were implemented in this analysis.

After the evaluation of the idle vibration levels for each of 117 experiments using the $L_{117}(3^8)$ orthogonal array table, the effect of each design variable on the idle vibration was analyzed through analysis of variance (ANOVA) [27]. ANOVA is a widely used statistical formula for comparing variances across the means (or average) of different variables. The sensitivity analysis results of the design variables with respect to the idle vibration within the specified design ranges are illustrated in Figure 20. The following design variables that affect idle vibration are listed in decreasing order of sensitivity: the rubber bushing stiffness of the radiator, the radiator mass, the lower hose stiffness of the intercooler, the intercooler mass, the lower hose stiffness of the radiator, the rubber bushing stiffness of the intercooler, the upper hose stiffness of the intercooler, and the upper hose stiffness of the radiator. In particular, the sensitivity analysis results depicted in Figure 20 are consistent with those of the parametric study presented in Figure 19.
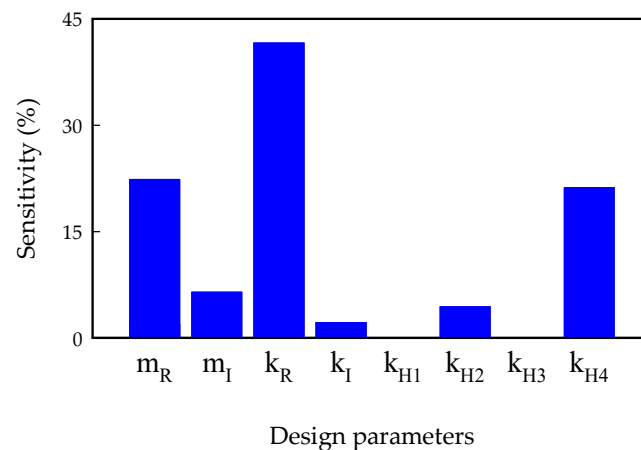


**Figure 20.** Results of the sensitivity analysis for the variations of each design variable.

To minimize the idle vibration level, the optimal design was implemented within the range constraints of the design variables. The design was optimized using the progressive quadratic response surface modeling (PQRSM) method, which is included in the commercial design optimization software package PIAnO [28]. To perform the design optimization using the eight design variables listed in Table 4, the idle vibration level was selected as the objective function, and these design variables were varied from their lower to upper limits, as depicted in Table 4. The idle vibration level obtained through the design optimization was 9 dB lower than the level yielded by the present design. The design variable values obtained from the design optimization are summarized in Table 4. In this table, the optimized values of the rubber bushing stiffness of the radiator and the intercooler mass represent the upper limits of the design ranges, whereas the optimized values of the lower hose stiffness of the radiator, the upper hose stiffness of the intercooler, and the lower hose stiffness of the intercooler comprise the lower limits. Conversely, the optimized values of the radiator mass, the upper hose stiffness of the radiator, and the rubber bushing stiffness of the intercooler do not exhibit any significant differences compared with the present design values.

A comparative study of the computed natural frequencies for the present and optimized designs reveals the modes that are affected by the optimization. Table 5 compares the natural frequencies computed via simulation for the present and optimal designs are compared in Table 5. In this table, the natural frequencies of the modes related to the powertrain and body floor do not change significantly. However, the natural frequencies of the bounce and roll modes of the radiator for the current design, which are 19.4 and 30.3 Hz, increased to 26.7 and 34.1 Hz in the optimal design. The increments in the natural frequencies for these modes are relatively large, 7.3 and 3.8 Hz. The natural frequency of the intercooler bounce mode in the current design, which is 31.0 Hz, is slightly reduced to 28.9 Hz in the optimal design. In other words, the natural frequencies of the modes for the

radiator and intercooler are more affected by the design optimization than the modes for the powertrain and body floor. This is because only design variables related to the radiator and intercooler were considered in the design optimization.

**Table 5.** Comparison of the natural frequencies for the present and optimal designs.

| Component | Mode | Natural frequency (Hz) | | |
| --- | --- | --- | --- | --- |
| | | Present design | Optimal design | Difference |
| Powertrain | Bounce mode | 6.7 | 6.6 | −0.1 |
| | Pitch mode | 15.3 | 15.3 | 0 |
| | Roll mode | 21.1 | 20.9 | −0.2 |
| Radiator | Bounce mode | 19.4 | 26.7 | 7.3 |
| | Roll mode | 30.3 | 34.1 | 3.8 |
| Intercooler | Bounce mode | 31.0 | 28.9 | -2.1 |
| Body floor | Bounce mode | 1.2 | 1.2 | 0 |
| | Pitch mode | 1.7 | 1.7 | 0 |
| | Bending mode | 25.2 | 24.1 | −1.1 |
| | Torsional mode | 28.0 | 28.1 | 0.1 |

The frequency response function of the dynamic model with the optimized design variables was compared with that of the model with the present design variables. Through this comparison, we investigated the reason of the dynamic model with the optimized variables exhibiting a lower idle vibration level than the model with the present variables. The frequency response functions for the dynamic models with the present and optimized design variables are compared in Figure 21, wherein the blue and red lines represent the frequency response functions for the present and optimal designs, respectively. As displayed in this figure, the frequency response function curves adjacent to the peaks of 1.2, 1.7, 6.7, and 15.3 Hz do not undergo significant changes, which are the natural frequencies of the bounce and pitch modes of the body floor and powertrain. However, a large variation can be observed in the curves corresponding to the idling frequency of 27.7 Hz. Owing to the design optimization, the frequency response function exhibits an anti-resonance point at idling frequency, significantly lowering the vibration level at the driver's seat. Therefore, the optimal design reduces the natural frequencies for the bounce modes of the radiator and intercooler (26.7 and 28.9 Hz, respectively) to a value proximate to the idling frequency (27.7 Hz), which causes the radiator and intercooler to act as vibration absorbers. Accordingly, a design, wherein the natural frequencies for the bounce modes of the radiator and intercooler are proximate to the idling frequency, is recommended to reduce the idle vibration on the driver's seat of a diesel SUV.
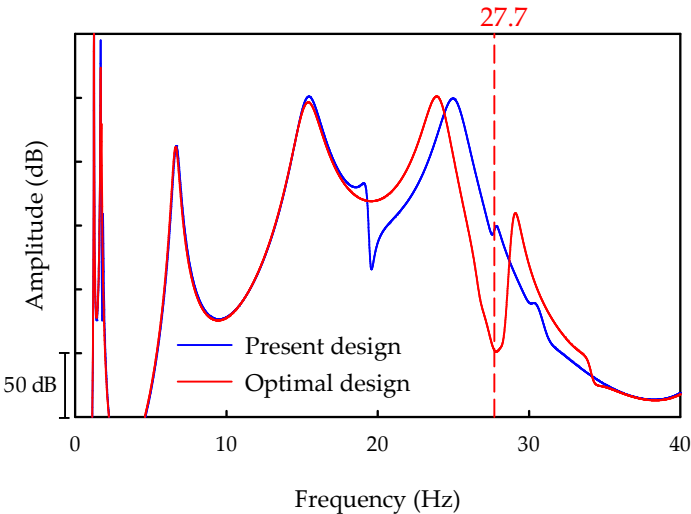
**Figure 21.** Comparison of the frequency response functions for the dynamic models with the present and optimal designs.

## 6. Conclusions

This paper proposes a method to reduce the idle vibration on the driver's seat of a diesel SUV by operating the radiator and intercooler as vibration absorbers. Through the ODS analysis, dynamic behaviors of the SUV components, such as the powertrain, radiator, and body floor, were identified in the idle engine state. In addition, modal tests were performed to obtain the natural frequencies and mode shapes of the SUV containing these components. Based on the results of the ODS analysis and modal tests, a dynamic model with 13 degrees of freedom was established, and the validity of the model was verified. The design variables of the SUV, which can be changed with relative ease, were selected, and their sensitivities on the idle vibration level were investigated. Furthermore, using these design variables, an optimal design was obtained to minimize the idle vibration level.

The results obtained in this study are summarized as follows:

1.  A dynamic model that can predict the idle vibration level on the driver's seat of a diesel SUV was established, wherein not only the rigid body modes of the powertrain, radiator, and intercooler but also the deformed modes such as the bending and torsional modes of the body floor were considered.
2.  The design variables sensitive to the idle vibration level within the changeable variable ranges are listed in the following decreasing order of sensitivity: the rubber bushing stiffness of the radiator, the radiator mass, the lower hose stiffness of the intercooler, the intercooler mass, the lower hose stiffness of the radiator, the rubber bushing stiffness of the intercooler, the upper hose stiffness of the intercooler, and the upper hose stiffness of the radiator.
3.  By using design variables related to the radiator and intercooler, design optimization was performed to reduce the idle vibration on the driver's seat, and the idle vibration was reduced by 9 dB through the optimization.
4.  The idle vibration level can be reduced by rendering the natural frequencies for the bounce modes of the radiator and intercooler proximate to the idle frequency. Accordingly, the radiator and intercooler act as vibration absorbers.

**Author Contributions:** Conceptualization, D.H.; methodology, S.R., D.K. and B.L.; software, S.R.; validation, S.R..; formal analysis, S.R. and D.K.; investigation, S.R., D.K. and B.L.; resources, D.H. and I.J.; data curation, S.R.; writing—original draft preparation, S.R.; writing—review and editing, S.R., J.C. and I.J.; visualization, S.R.; supervision, J.C.; project administration, J.C. All authors have read and agreed to the published version of the manuscript.

**Data Availability Statement:** Not applicable here.

**Conflicts of Interest:** The authors declare no conflict of interest.

## References

1.  Zheng, Q.; Srinivasan, K.; Rizzoni, G. Optimal engine-transmission control of neutral-idle clutch application. *JSAE Review* **2001**, *22*, 463–472.
2.  Kim, D.E.; Park, J. Application of adaptive control to the fluctuation of engine speed at idle. *Inf. Sci.* **2007**, *177*, 3341–3355.
3.  Fu, T.; Rakheja, S.; Shangguan, W.B. Design of a hybrid proportional electromagnetic dynamic vibration absorber for control of idling engine vibration. In Proceedings of the Institution of Mechanical Engineering Part D-Journal of Automobile Engineering **2020**, *234*, 56–70.
4.  Shen, H.M; Tang, P.; Bian, F.; Wu, X.W.; Zhao, W.J.; Hu, L.L. An experimental study of vehicle 1st order vibration improvement at engine idle. *Int. J. Acoust. Vib.* **2020**, *25*, 542–548.
5.  Shangguan, W.B.; Liu, X.L.; Yin, Y.; Rakheja, S. Modeling of automotive driveline system for reducing gear rattles. *J. Sound Vib.* **2018**, *416*, 136–153.

6.	Yucesan, A.; Sezer, S. Vibration isolation with clutch disk pre-damper mechanism for the idle rattle phenomenon, *J. Vib. Control* **2018**, *24*, 1518–1534.
7.	Brancati, R.; Rocca, E.; Russo, R. Gear rattle reduction in an automotive driveline by the adoption of a flywheel with an innovative torsional vibration damper. In Proceedings of the Institution of Mechanical Engineers Part K-Journal of Multi-Body Dynamics **2019**, *233*, 777–791.
8.	Chen, L.; Shi, W.; Chen, Z. Research on damping performance of dual mass flywheel based on vehicle transmission system modeling and multi-condition simulation. *IEEE Access* **2020**, *8*, 28064–28077.
9.	Choi, S.B.; Song, H.J. Vibration control of a passenger vehicle utilizing a semi active ER engine mount. *Veh. Syst. Dyn.* **2002**, *37*, 193–216.
10.	Azadi, M.; Behzadipour, S.; Faulkner, G. Introducing a new semi-active engine mount using force controlled variable stiffness. *Veh. Syst. Dyn.* **2013**, *51*, 721–736.
11.	Guo, R.; Zhou, Z.W. Non-linear modeling and parameter identification of semi-active engine mounts with air spring. *J. Vib. Acoust.-Trans. ASME* **2020**, *142*, 011018.
12.	He, S.; Chen, B.; Jiang, Z.; Wang, Y.; Liu, F. Control of steering wheel idle jitter based on optimization of engine suspension system with verifications using multi-sensor measurement. *Int. J. Dist. Sensor Net.* **2018**, *14*, 1550147718782373.
13.	Lim, J.; Sim, W.; Yun, S.; Lee, D.; Chung, J. Reduction of vibration forces transmitted from a radiator cooling fan to a vehicle body. *J. Sound Vib.* **2018**, *419*, 183–199.
14.	Wang, Q.; Ren, C.; Zhou, J.; Zhang, L. The double-delay reducing vibration control for five-degree-of-freedom half-vehicle model in idle condition. *J. Low Freq. Noise Vib. Act. Control* **2020**, *39*, 203–215.
15.	Bohn, C.; Cortabarria, A.; Hartel, V.; Kowalczyk, K. Active control of engine-induced vibrations in automotive vehicles using disturbance observer gain scheduling. Control Eng. Pract. **2004**, *12*, 1029–1039.
16.	Han, T.; Huang, C.; Tan, A.C.C. Experimental and finite element analysis to identify the source of vibration of a coach. *Eng. Fail. Anal.* **2014**, *44*, 100–109.
17.	Kim, K.C.; Kim, C.M. Analysis process of a steering system using a concept model for idle vibration. *Int. J. Auto. Technol.* **2008**, *9*, 337–346.
18.	Wang, C.Y.; Zhang, Y.Q.; Zhao, W.Z. Multi-objective optimization of a steering system considering steering modality. *Adv. Eng. Soft.* **2018**, *126*, 61–74.
19.	He, S.; Tang, T.; Ye, M.; Xu, E.; Jiang, Z. A multi-point iterative analysis method for vibration control of a steering wheel at idle speed. *IEEE Access* **2019**, *7*, 88399–88417.
20.	Tang, T.; He, S.; Ye, M.; Xu, E.; Zheng, W. Research on a multinode joint vibration control strategy for controlling the steering wheel of a commercial vehicle. *Shock Vib.* **2020**, 7146828.
21.	Schwarz, B.J.; Richardson, M.H. *Introduction to operating deflecting shapes*. CSI Reliability Week, Orlando, FL, USA, October 1999.
22.	Taylor, R.K.; Bashford, L.L.; Schrock, M.D. Methods for measuring vertical tire stiffness. *Trans. ASAE* **2000**, *43*, 1415–1419.
23.	Jing, L.; Wu, L.; Li, X.; Zhang, Y. Study on kinematic and compliance test of suspension. IOP Conference Series: *Mat. Sci. Eng.* **2017**, *231*, 012186.
24.	Nigus, H. Kinematics and load formulation of engine crank mechanism. *Mech. Mater. Sci. Eng. J.* **2015**, *ISSN* 2412-5954.
25.	Lichty, L.C. *Combustion Engine Processes*, 6th ed.; McGraw-Hill, New York, USA, 1967.
26.	Cao, Y.; Cao, D.; He, G.; Ge, X.; Hao, Y. Modelling and vibration analysis for the multi-plate structure connected by nonlinear hinges. *J. Sound Vib.* **2021**, *492*, 115809.
27.	Scheffé, H. *The Analysis of Variance*, 1st ed.; Wiley, New York, USA, 1959.
28.	PIAnO User's Manual, Framax Inc. Seoul, 2008.